nonlinear optical system (*7*) incorporating a different type of nonlinearity and different dimensions and geometry. This similarity implies that the modal selection is of generic type and has little dependence on the specific parameters. Second, the CGL equation describing the nonlinear microcavity supports dark solitons (although the medium is self-focusing); and the ordered arrays of optical vortices, while propagating in the nonlinear cavity, can be modeled as arrays of dark (vortex) solitons. Their particlelike behavior, together with the possibility of deriving their soliton-soliton and soliton-device boundary forces, is a preferable direction for exploring the stability (and possibly the control) of these patterns.

We demonstrated the generation of complex spatial patterns and optical vortices crystals in broad-area VCSELs and showed that these patterns can be interpreted by the concept of transverse locking. The locking was possible because of the relatively small frequency spacing between specific modes of the cavity (almost wavelength-degenerated). The patterns appeared in both round and rectangular lasers, and they preserved their lateral distribution (with proper scaling) in the far field as well. The theoretical results revealed that the only combinations obtainable with the model of the VCSEL nonlinear cavity were the same specific mode combinations that were observed experimentally. The ability to spontaneously generate controlled and stable vortex arrays in a miniature cavity device is very appealing for applications of dynamic optical storage and processing.

References and Notes

1. V. Yu. Bazhenov, M. S. Soskin, M. V. Vasnetsov, *J. Mod. Opt.* **39**, 985 (1992); G. Indebetouw, *ibid.* **40**, 73 (1993); I. V. Basistiy, *et al.*, *Opt. Comm.* **103**, 422 (1993); J. F. Nye and M. V. Berry, *Proc. R. Soc. London Ser. A*, **336**, 165 (1974).
2. K. T. Gahagan and G. A. Swartzlander, *J. Opt. Soc. Am. B* **16**, 533 (1999).
3. W. J. Firth and A. J. Scroggie, *Europhys. Lett.* **26**, 521 (1994).
4. G. D'Alessandro and W. J. Firth, *Phys. Rev. A.* **46**, 537 (1992).
5. D. Michaelis, U. Peschel, F. Lederer, in *QELS'97* (Optical Society of America, Baltimore, MD, 1997), pp. 70–71.
6. W. J. Firth, A. J. Scroggie, G. S. McDonald, *Phys. Rev. A* **46**, R3609 (1992).
7. M. Brambila *et al.*, *ibid.* **43**, 5090 (1991).
8. M. Orenstein, *et al.*, *Appl. Phys. Lett.* **56**, 2384 (1990).
9. P. Coullet, L. Gill, F. Rocca, *Opt. Comm.* **73**, 403 (1989).
10. Ordered arrays of dark hexagons were predicted for Kerr medium by D'Alessandro and Firth (*4*).
11. G. P. Agrawal and N. K. Dutta, *Long Wavelength Semiconductor Lasers* (Van Nostrand Reinhold, New York, 1986).
12. J. Scheuer, D. Arbel, M. Orenstein, personal communication.
13. A. Yariv, *Optical Electronics* (Saunders, Philadelphia, PA, ed. 4, 1991).
14. The Gauss-Laguerre functions are the transverse solutions of the paraxial wave equation. The functions are

$$A_{p0}(r,\varphi) = \frac{2}{\sqrt{2\pi}} L_p^0(2r^2)\cdot e^{-r^2}; A_{plj}(r,\varphi) = \frac{2}{\sqrt{2\pi}}(2r^2) = \left(\frac{p!}{(p+1)!}\right)^{1/2}\cdot L_p^1(2r^2)\cdot e^{-r^2} \times \begin{cases} e^{+il\varphi} & j=1 \\ e^{-il\varphi} & j=2 \end{cases}$$

where $p = 0, 1, \ldots$ is the radial index; $l = 0, 1, \ldots$ is the angular index; r is the radial coordinate normalized by the beam waste; and $L^1{}_p$ is Laguerre polynomials. The electrical field is represented by $\varepsilon(t) = \sum_n E_n(t)\cdot\Psi_n(r,\varphi)$, where Ψ_n is the Gauss-Laguerre modes. The functions satisfying $2p + l =$ constant have the same propagation constant (that is, the same wavelength in the cavity) and form a wavelength-degenerated family.

15. L. A. Coldern and S. W. Corzine, *Diode Lasers and Photonic Integrated Circuits* (Wiley-Interscience, New York, 1995).
16. An additional control parameter, σ, is included in our analysis to correctly describe a local width imposed by either the boundary conditions or local inhomogeneity. The width parameter transforms the uniformly distributed spectral models of an unbounded problem into a banded spectrum. The almost-degenerated wavelength modes within each band are readily locked by the medium nonlinearity to form the complex field pattern. Both the lateral inhomogeniety and the complex nonlinear medium are the required ingredients for the pattern formation. This result is generally applicable to vortex formation in various fields of science. To the best of our knowledge, all such patterns reported previously (experimental and theoretical) were obtained in bounded nonlinear systems (including periodic boundaries) (*3–6, 10*). The specific details of the width parameter in our system are related to the inhomogeneous pumping and thermally induced index gradient (thermal lensing) that are well known for semiconductor lasers.
17. We thank the Israel Ministry of Science and Technology for partially supporting this research and one of the reviewers for helpful remarks.

13 January 1999; accepted 1 June 1999

All-Polymer Optoelectronic Devices

Peter K. H. Ho, D. Stephen Thomas, Richard H. Friend, Nir Tessler*

Composites of nanoparticles and conjugated polymers that exhibit composition-tunable optical constants have been developed for use in semiconducting photonic structures. For example, the 550-nanometer wavelength in-plane refractive index of poly(p-phenylenevinylene)–silica composites can be tailored over the range of 1.6 to 2.7, allowing efficient distributed Bragg reflectors and waveguides to be fabricated. Low levels of chemical doping improve electrical conductivity through these structures without detriment to their photonic properties. Exemplifying these concepts, all-polymer microcavities and microcavity light-emitting diodes were demonstrated. Appropriate confinement of photons and electron-hole pairs in these organic semiconductor-based structures can be achieved.

Organic semiconductor devices are receiving considerable attention because of the immense tailorability and processing advantages of conjugated polymers (*1–4*). Recent developments in ink-jet printing, microcontact printing, and other soft lithographies (*5*) have further improved their potential for low-cost fabrication of large-area integrated devices on both rigid and flexible substrates. However, steps toward all-organic optoelectronic devices (*1, 2*) have been hampered by the lack of appropriate photonic building blocks that have a sufficient refractive index contrast and that can support a useful current density.

This is because, to a large extent, the index contrast between organic polymers is limited by the similar refractive powers of their constituent structural units (*6*). Even if the desired contrast can be obtained, the discontinuity of charge transport levels across the interface still potentially complicates carrier motion across the junction. Hence, there is an incentive to find a general scheme that allows the optical constants to be manipulated separately from other electronic and transport properties of the material.

One successful scheme is to form nanocomposites of the polymer with well-dispersed wide bandgap nanoparticles. The method comprises a microemulsion nanoparticle synthesis (*7*), followed by surface functionalization, and homogeneous blending with the polymer solution for subsequent processing. Using this approach, we obtained thin films of the semiconducting poly(p-phenylenevinylene)–silica (PPV-SiO_2) composite that combine a wide index tunability with little Mie scattering, in contrast to previous work (*8, 9*).

Although PPV and SiO_2 are selected because of their respective high (n_{550} = 2.3 to 2.7, depending on processing) and low (n_{550} = 1.45) refractive indices at a wavelength of 550 nm, the method can readily be generalized to include other matrix polymers (for example, polyfluorenes) and inorganic particles (for example, high-index ZrO_2). Repeated solution-deposition and insolubilization by thermal processing or cross-linking can then be used to

Cavendish Laboratory, Madingley Road, Cambridge CB3 0HE, UK.

*To whom correspondence should be addressed. E-mail: nt202@phy.cam.ac.uk

form the polymer photonic structures bearing spatially modulated refractive index profiles.

In addition, these structures must be doped (*10*) to obtain sufficient electrical conductivity for a useful current density ($\geq$1 mA/cm^2) to be injected through their thicknesses, which are of the order of a few optical wavelengths (that is, ~1 μm). The common approach of exhaustive protonic or oxidative positively charged doping to a high carrier density of 10^{20} to 10^{21} cm^{-3} would be unsuitable because the induced subgap absorption degrades the photonic structure (*11*). Controlled chemical doping to the level of 10^{17} to 10^{19} cm^{-3} [that is, 0.1 to 1 mole percent (mol%)] could be adequate because the bulk carrier density under normal driving conditions is below 10^{17} cm^{-3} (*12*). For this, we extended an earlier strategy (*11*) to introduce a small fraction of phenylphosphonate dopant anions to the precursor PPV.

Conventional photonic structures are derived from inorganic insulators such as SiO_2 and Si_3N_4 or from semiconductors such as AlAs and GaAs if current flow is desired. They provide a valuable means to spatially and spectrally direct the optical output of optoelectronic devices, including light-emitting diodes and laser diodes, thereby greatly enhancing their performance (*13, 14*). A microcavity provides control over emission characteristics such as wavelength, spectral purity, direction, and intensity of embedded emitters by altering the photon density of states inside the cavity (*13–16*). To show that organic photonic structures can emulate these characteristics while retaining their own processing and color-tuning advantages, we fabricated microcavity light-emitting diodes (mcLEDs) in which the emitter layer and the distributed Bragg reflector (DBR) of the microcavity are made from semiconducting polymers. When a suitable polymer emitter layer is spaced between two polymer DBRs, we also obtained an all-polymer microcavity in which the embedded emitter can be optically excited.

In a mcLED, electrically injected electrons and holes recombine inside an optical cavity so that radiative decay of the excitons are coupled to the cavity modes (*14*). Previously, mcLEDs of organic emitters were fabricated on electron beam–evaporated inorganic DBRs (*17–19*). Because these are electrically insulating, the injecting anode has to be placed inside the cavity, degrading its quality factor. With semiconducting DBRs, the anode can be located outside the cavity.

SiO_2 nanoparticles with a diameter of 50 Å were grown by alkaline $SiCl_4$ hydrolysis in a dioctylsulfosuccinate-stabilized, water-in-cyclohexane reverse microemulsion. After purification, the particles were capped with a 10:1 mixture of ethyl and ammoniopropyl groups for a positively charged surface with lowered hydrophilicity. The cationic SiO_2 dispersion was then mixed with the tetrahydrothiophenium-precursor of poly(p-phenylenevinylene) (PPV-THT-Cl) in methanol to give a range of compositions. These stable transparent mixtures could be spin-cast and thermally converted to uniform films of the PPV-SiO_2 nanocomposites.

Transmission spectroscopy of these films revealed that the nanoparticles are well dispersed (Fig. 1A). There is no detectable scattering background arising from particle agglomeration on a length scale exceeding about one-tenth of the optical wavelength in the film. Tapping mode atomic force microscopy also shows the absence of large-scale agglomerated structures. The average microroughness determined over an area of 25 μm^2 for films that are 1000 to 2000 Å thick is 60 to 140 Å.

The π-π* absorption maxima of these composites undergoes a small blue shift of 0.15 eV from 2.95 eV in the neat film to 3.10 eV in the composite with 50 volume % of SiO_2 (Fig. 1A). Photoluminescence spectroscopy that probes the longest conjugation segments similarly reveals a small blue shift in emission energies. Zero-phonon emission peak shifts 0.05 eV, from 2.40 eV in the neat film to 2.45 eV in the 50 volume % composite. Despite a possible physical disruption

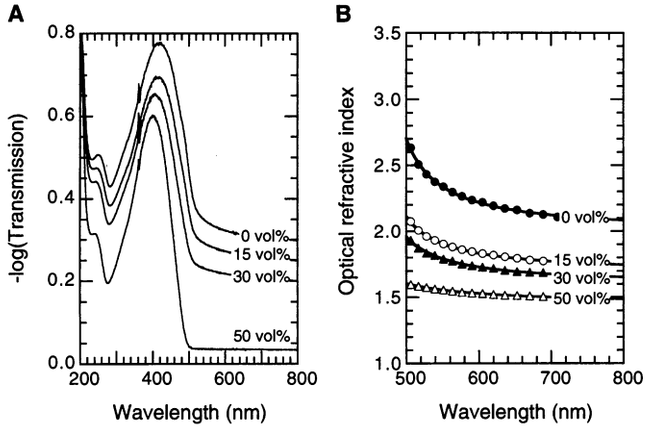

Fig. 1. (**A**) Uncorrected transmission spectra of PPV-SiO_2 nanocomposite films on fused silica. The plots for 30, 15, and 0 volume % of SiO_2 are vertically offset in multiples of 0.05 for clarity. The flat transmission response of the 50 volume % SiO_2 composite outside its absorption edge attests to the weak optical dispersion and absence of optical scattering in this material. With decreasing SiO_2 volume percent, a reflection loss tail emerges outside the absorption edge. (**B**) Refractive index dispersion of the PPV-SiO_2 nanocomposite films. The symbol plots were calculated from spectroellipsometry data recorded at a 55° incidence angle on fused silica to weigh them strongly to the in-plane optical response. The curves are a Sellemier fit to the symbol plots.

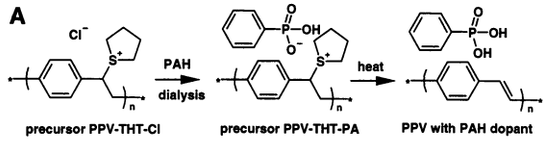

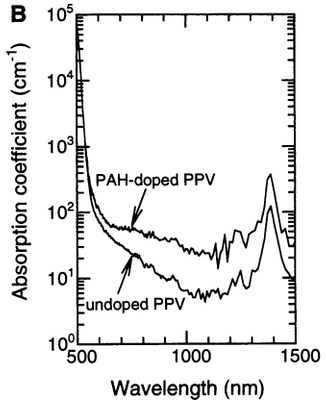

Fig. 2. (**A**) Low-level chemical doping of PPV with PAH. n represents the number of repeat units on a polymer chain. (**B**) Absorption spectra of an undoped PPV film and a film nominally doped with 10 mol% PA$^-$ on fused silica, measured by photothermal deflection spectroscopy. The increased subgap absorption over 600 to 1200 nm due to charge-defect transitions is discernible but not excessive so that the photonic structure is not degraded. The 1380-nm feature is due to a hydroxyl-stretching overtone in the silica substrates.

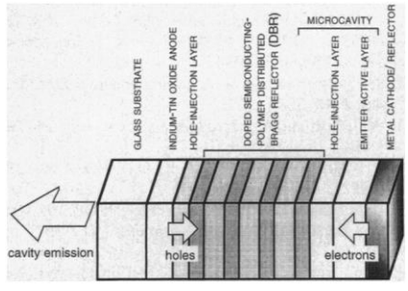

Fig. 3. Schematic of the polymer mcLED with an optical cavity defined by a 3.5-period PPV DBR and a Ca/Al mirror. The DBR comprises quarter-wave layers of neat PPV (570 Å and n_{550} = 2.75) and PPV dispersed with 50 volume % of SiO_2 (690 Å and n_{550} = 1.65), processed at 220°C. The cavity comprises a PSS-enriched PEDOT:PSS hole-injection layer (730 Å and n_{550} = 1.7) and an F8BT emitter layer (1090 Å and n_{550} = 1.8). Confinement of photons to the cavity length results in a discrete photon density of states. Confinement of electron-hole capture to the emitter layer near the cavity field antinode results in efficient radiative coupling to the resonant cavity mode.

of the π conjugation induced by the nanometer-sized particles, the effective π-π^* gap and the semiconducting properties of PPV appear to be relatively unaffected.

Both the in-plane refractive index and its optical dispersion (wavelength-dependent change of refractive index) decrease drastically (Fig. 1B) with increasing SiO_2 loading (volume percent in parentheses): n_{550} = 2.35 (0), 1.90 (15), 1.80 (30), and 1.55 (50). This huge index contrast generated between neat PPV and the various PPV-SiO_2 composites could be exploited to build efficient DBRs and optical waveguides operating in the green spectral region.

The reduction of the effective refractive index n_e of the composite is expected from effective medium averaging of the PPV host and the SiO_2 guest (n_{550} = 1.45). For two nonabsorbing components with volume fractions f_i and refractive indices n_i, the Bruggemann effective medium approximation gives $f_1[(n_1^2 - n_e^2)/(n_1^2 + 2n_e^2)] + f_2[(n_2^2 - n_e^2)/(n_2^2 + 2n_e^2)] = 0$.

Data modeling, however, reveals another important contribution to the pronounced index lowering. The in-plane refractive index of the polymer matrix itself decreases with SiO_2 loading (volume percent in parentheses): n_{550}^{matrix} = 2.35 (0), 2.05 (15), 1.95 (30), and 1.70 (50). Its origin is attributed to void formation and the disruption of in-plane chain alignment in the presence of a high particle density.

Unlike the behavior of larger or more agglomerated particles or both (*8, 20*), charge transport is substantially impeded in these composite films. We tested the transport property of the film in a diagnostic diode configuration (*21*) comprising an indium–tin oxide (ITO) anode, a hole-injection layer with conducting-polymer polystyrenesulfonate-doped poly(3,4-ethylenedioxythiophene) (PEDOT:PSS), the test layer, and a Ca cathode. A 69-nm-thick PPV-SiO_2 film with 50 volume % nanoparticles yields only 0.04 mA/cm^2 at an applied field of 1.2 MV/cm, several orders of magnitude less than the current yield of the reference diode with a 114-nm-thick PPV film (5 mA/cm^2 at 0.7 MV/cm).

This increased resistance may be related to several factors, including carrier scattering, pinning, and trapping at the polymer-nanoparticle interface, although the last factor may be the least important owing to the unfavorable energy levels of SiO_2. When carrier mobility is suppressed, injection will also be hindered owing to an increased backflow of injected carriers at the contact.

To raise the diode current, we introduced phenylphosphonic acid (PAH) to the PPV layers by dialysis exchange of the Cl^- counterions for phenylphosphonate anions (PA^-) (Fig. 2A). The modified PPV precursor polymer (PPV-THT-PA) was then diluted to 10 mol% PA^- with PPV-THT-Cl. During the second stage of thermal processing (>130°C) to form the π conjugation of PPV, both HCl and PAH are eliminated. Because PAH is much less volatile than HCl, it is retained to a greater extent in the film, as confirmed by x-ray photoemission spectroscopy. The actual doping level (*11, 22*) may, however, be much smaller than the dopant concentration because not all of the PAH molecules become ionized.

Because it was difficult to characterize doping levels in a multilayer structure, we studied analogously doped single-layer PPV films (Fig. 2B) using photothermal deflection spectroscopy (*23*). With a polaron absorption cross section of 10^{-16} to 10^{-15} cm^2 (*24*), the subgap absorption coefficient of 10^2 cm^{-1} corresponds to a polaron concentration of 10^{17} to 10^{18} cm^{-3}. This low-level doping (0.1 to 0.01 mol%) already tremendously improves carrier transport through the photonic structures. However, we estimate that another order of magnitude increase in doping level should be possible to further improve carrier transport without degrading the photonic structure.

The structure of the polymer mcLEDs is shown in Fig. 3. The PPV DBR was first formed over a PEDOT:PSS-coated ITO substrate by repeated spin-casting and baking at 120°C of the appropriate polymer solutions (a doped PPV precursor alternating with a SiO_2-dispersed precursor). The completed multilayer structure was then heated to 220°C for 2 hours in an Ar atmosphere to form a periodic quarter-wave stack of high-index PPV and low-index PPV-SiO_2 layers. Peak reflectance of the 3.5-period DBR in air exceeds 75% at the Bragg wavelength of 550 nm, whereas that of the 5.5-period DBR exceeds 90%.

To form the cavity layers, we deposited a second PEDOT:PSS hole-injection layer followed by a poly(dioctylfluorene-co-benzothiadiazole) (F8BT)–based emitter layer. Finally, an Al-capped Ca cathode/reflector was thermally evaporated to define diodes with an active area of 3 to 4 mm^2. When forward biased, the polymer DBR transports holes injected from the transparent ITO anode to the PEDOT:PSS hole-injection layer in the cavity. From there, holes are injected into the F8BT emitter layer where recombination with electrons injected from the Ca cathode/reflector occurs. The recombination zone is spaced near the antinode of the cavity optical field by the PEDOT:PSS layer for optimal radiative coupling to the cavity mode. Appropriate confinement of both the electron-hole pairs and the emitted photons are thus crucial for the mcLED to operate properly.

The electroluminescence emission of the mcLED with a 3.5-period organic DBR is resonant with the cavity mode at 530 nm (Fig. 4A). The emission width ($\Delta\lambda$) of 25 nm is considerably narrower than the natural emission width ($\Delta\lambda_0$) of 100 nm measured in regular F8BT LEDs. Because of the wide $\Delta\lambda_0$, no substantial enhancement of the integrated cavity emission or its redistribution into the forward direction can be expected (*18, 19*). With optical field penetration into the DBR, the effective mode number (m_{eff}) is 3. The cavity finesse given by $\lambda/(m_{eff}\Delta\lambda)$ is thus 7.1, which is slightly smaller than the theoretically predicted finesse (*25*) of 10 for DBR and metal reflectances of 65 and 85%, respectively. This could be related to a cavity-width fluctuation across the device area. For a current density of 2.5 mA/cm^2, the required drive voltage is 50 V in this prototype device. Increasing the DBR doping level should enable much lower drive voltages to be attained.

The on-axis luminous efficiency of the mcLED reaches 2.5 cd/A (Fig. 4B), comparable to regular F8BT LEDs (2 to 5 cd/A). The relative efficiency of this mcLED suggests that, despite the long path length of holes, adequate confinement of the electron-hole recombination to the emitter layer has been achieved.

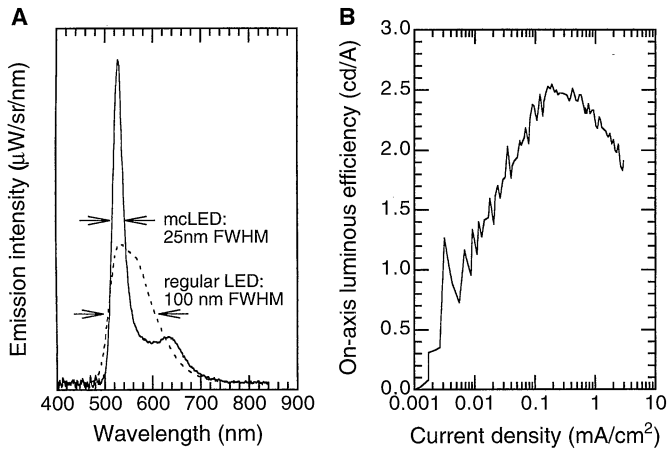

Fig. 4. (A) On-axis electroluminescence spectra of the mcLED (solid line) and a regular LED (dashed line). Emission of this mcLED is largely restricted to the resonant cavity mode at a wavelength of 530 nm, with a small leakage emission where the DBR reflectance ends. **(B)** On-axis luminous efficiency of the mcLED plotted against diode current density. This prototype mcLED has a similar external quantum efficiency as the regular LED counterpart but emits light with a better spectral purity.

To show that the emitted photons originate from within the cavity, we tuned the cavity off-resonance by changing the thickness of the active layer and found no resonant emission. When the output reflector is replaced by a 5.5-period PPV DBR, we obtain a higher cavity finesse ($\Delta\lambda$ = 16 nm), but at the expense of efficiency. Moreover, the large optical dispersion of the PPV DBR should also be useful to reduce the off-axis color shift (*26*).

Our approach allows the refractive index of polymer semiconductors to be varied without altering the energies of their electron- and hole-transport states, so that charge transport across the layer interfaces remains facile. This contrasts with the situation when different semiconductors are used, for example, in GaAs/AlGaAs DBRs (*27*).

We conclude that separate manipulation and thus orthogonal design of the optical, electronic, and transport properties of semiconducting polymers are feasible. This may enable the fabrication of a new generation of organic semiconductor optoelectronic devices with refractive index and carrier transport level profiles that are functional.

References and Notes

1. A. Dodabalapur *et al.*, *Appl. Phys. Lett.* **73**, 142 (1998).
2. H. Sirringhaus, N. Tessler, R. H. Friend, *Science* **280**, 1741 (1998).
3. A. J. Heeger, *Solid State Commun.* **107**, 673 (1998).
4. R. H. Friend *et al.*, *Nature* **397**, 121 (1999).
5. S. Brittain, K. Paul, X.-M. Zhao, G. Whitesides, *Phys. World* 1998, 31 (May 1998).
6. D. W. V. Krevelen, *Properties of Polymers: Their Correlation with Chemical Structure, Their Numerical Estimation and Prediction from Additive Group Contributions* (Elsevier, Amsterdam, ed. 3, 1990).
7. M. P. Pileni, *J. Phys. Chem.* **97**, 6961 (1993).
8. S. A. Carter, J. C. Scott, P. J. Brock, *Appl. Phys. Lett.* **71**, 1145 (1997).
9. B. J. Schwartz, F. Hide, M. A. Díaz-García, M. R. Andersson, A. J. Heeger, *Philos. Trans. R. Soc. London Ser. A* **355**, 775 (1997).
10. A. Yamamori, C. Adachi, T. Koyama, Y. Taniguchi, *Appl. Phys. Lett.* **72**, 2147 (1998).
11. C. C. Han and R. L. Elsenbaumer, *Synth. Met.* **30**, 123 (1989).
12. N. Tessler, N. T. Harrison, R. H. Friend, *Adv. Mater.* **10**, 64 (1998).
13. H. Yokoyama, *Science* **256**, 66 (1992).
14. E. F. Schubert *et al.*, *ibid.* **265**, 943 (1994).
15. D. G. Lidzey *et al.*, *Nature* **395**, 53 (1998).
16. T. Granlund *et al.*, *Chem. Phys. Lett.* **288**, 879 (1998).
17. T. Nakayama, Y. Itoh, A. Kakuta, *Appl. Phys. Lett.* **63**, 594 (1993).
18. R. H. Jordan, L. J. Rothberg, A. Dodabalapur, R. E. Slusher, *ibid.* **69**, 1997 (1996).
19. J. Grüner, F. Cacialli, R. H. Friend, *J. Appl. Phys.* **80**, 207 (1996).
20. P. W. M. Blom, H. F. M. Schoo, M. Matters, *Appl. Phys. Lett.* **73**, 3914 (1998).
21. J. C. Carter *et al.*, *ibid.* **71**, 34 (1997).
22. A. Sakamoto, Y. Furukawa, M. Tasumi, *J. Phys. Chem. B* **101**, 1726 (1997).
23. A. C. Arias, M. G. Granström, D. S. Thomas, R. H. Friend, *Phys. Rev. B*, in press.
24. M. G. Harrison, K. E. Ziemelis, R. H. Friend, P. L. Burn, A. B. Holmes, *Synth. Met.* **55**, 218 (1993).
25. E. F. Schubert, N. E. J. Hunt, R. J. Malik, M. Micovic, D. L. Miller, *J. Lightwave Technol.* **14**, 1721 (1996).
26. N. Tessler, S. Burns, H. Becker, R. H. Friend, *Appl. Phys. Lett.* **70**, 556 (1997).
27. K. Tai, L. Yang, Y. H. Wang, J. D. Wynn, A. Y. Cho, *ibid.* **56**, 2496 (1990).

28. This work has been partially supported by the European Commission under Brite-Euram contract BRPR-CT97-0469 ("OSCA") and by the Engineering and Physical Sciences Research Council. We thank Cambridge Display Technology (Cambridge, UK) for materials, R. A. L. Jones and A. Wehrum for the spectroscopic ellipsometer facility, and E. P. Woo at The Dow Chemical Company (Midland, MI) for support. P.K.H.H. is on study leave from the National University of Singapore and thanks St. John's College (Cambridge, UK) and the Institute of Materials Research and Engineering (Singapore) for funding.

25 March 1999; accepted 8 June 1999

Role of Fluids in Faulting Inferred from Stress Field Signatures

Jeanne L. Hardebeck* and Egill Hauksson

The stress orientation signature of weak faults containing high-pressure fluids has been observed for segments of the San Andreas fault system in southern California. The inferred lithostatic fluid pressures extend into the surrounding relatively intact rock in a zone scaling with the width of the interseismic strain accumulation. Repeated strain-related fracturing and crack sealing may have created low-permeability barriers that seal fluids into the network of currently active fractures.

It is crucial for understanding fault evolution and the dynamics of large earthquakes to determine why numerous major faults, including the San Andreas in California, are weak (*1–3*). Fault zone fluids at high (~lithostatic) pressures could lower the effective normal stress on a fault, decreasing its shear strength (*2*). Alternatively, weak faults may contain inherently weak materials, although laboratory testing has eliminated most candidate minerals (*4*). A third model is dynamic weakening, in which fault strength reduces during slip (*5*).

Each model contains predictions about the orientation of the maximum principal stress axis σ_1. For a strong fault, σ_1 should be at ~30° to the fault plane (*3*). If the fault is dynamically weak, σ_1 is predicted to be at a higher angle, which is controlled by the frictional resistance during slip. Some rotation toward lower angles near the fault may occur because of interseismic loading of the fault. However, if typical interseismic stress changes of ~5 MPa (*6*) are to rotate the stress field $\geq$10°, the background deviatoric stress must be $\leq$15 MPa (*7*). Crustal stress is typically near the laboratory-predicted frictional strength of rock (*8*), which, over seismogenic depths, corresponds to an average deviatoric stress of ~50 MPa (*9*). Rotations of $\geq$10° therefore imply weak material.

A stress state is predicted to develop inside a fault zone of weak materials (either inherently weak or weakened by high-pressure fluids) that is distinct from that outside (*10, 11*). An increase in fault-parallel stress inside the fault zone, which suppresses hydrofracture in the case of high fluid pressure, rotates the principal stress axes (Fig. 1). The model predicts σ_1 to be at high angles to the fault ($\geq$60°) outside the fault zone and at lower angles ($\leq$60°) inside (Fig. 1C).

We use stress orientations determined from earthquake focal mechanisms to look for evidence of stress rotation across the San Andreas fault system in southern California, which consists of three major right-lateral strike-slip faults: the San Andreas (SAF), San Jacinto (SJF), and Elsinore (EF). We have compiled a catalog of about 50,000 earthquakes recorded by the California seismic networks (Fig. 2). The earthquakes along eight profiles across relatively straight segments of the SAF, SJF, and EF are inverted for the direction of maximum horizontal stress σ_H (Figs. 2 and 3). We interpret our observations in terms of the models presented above. For fault segments that parallel the relative plate motion (Fig. 3, profiles A, F, G, and H), far-field σ_H is typically ~60° to the fault trend. However, within 2 to 5 km of the Parkfield and Indio segments of the SAF (Fig. 3, A and G), the northern and southern SJF (Fig. 3, F and H), and the central and southern EF (Fig. 3, G and H), σ_H is at ~40° to the fault trend.

In the region of the compressional bend in the SAF (profiles B, C, D, and E) far-field σ_H is typically ~90° to the fault trend. Near the Fort Tejon (Fig. 3B) and San Bernadino (Fig. 3D) segments of the SAF, however, σ_H is at ~40° to the fault trend. The zone of stress rotation across the Fort Tejon segment is 20 to 30 km wide, whereas that across the San Ber-

Seismological Laboratory, MC 252-21, California Institute of Technology, Pasadena, CA 91125, USA.

*To whom correspondence should be addressed. E-mail: jlh@gps.caltech.edu